

UC Santa Barbara

UC Santa Barbara Previously Published Works

Title

Effect of cholesterol nanodomains on monolayer morphology and dynamics.

Permalink

<https://escholarship.org/uc/item/9pj3f088>

Journal

Proceedings of the National Academy of Sciences, 110(33)

Authors

Kim, Kyuhan
Choi, Siyoung
Zell, Zachary
et al.

Publication Date

2013-08-13

DOI

10.1073/pnas.1303304110

Peer reviewed

Effect of cholesterol nanodomains on monolayer morphology and dynamics

KyuHan Kim^a, Siyoung Q. Choi^b, Zachary A. Zell^a, Todd M. Squires^a, and Joseph A. Zasadzinski^{b,1}

^aDepartment of Chemical Engineering, University of California, Santa Barbara, CA 93106; and ^bDepartment of Chemical Engineering and Materials Science, University of Minnesota, Minneapolis, MN 55455

Edited by David A. Weitz, Harvard University, Cambridge, MA, and approved June 26, 2013 (received for review February 20, 2013)

At low mole fractions, cholesterol segregates into 10- to 100-nm-diameter nanodomains dispersed throughout primarily dipalmitoylphosphatidylcholine (DPPC) domains in mixed DPPC:cholesterol monolayers. The nanodomains consist of 6:1 DPPC:cholesterol “complexes” that decorate and lengthen DPPC domain boundaries, consistent with a reduced line tension, λ . The surface viscosity of the monolayer, η_s , decreases exponentially with the area fraction of the nanodomains at fixed surface pressure over the 0.1- to 10-Hz range of frequencies common to respiration. At fixed cholesterol fraction, the surface viscosity increases exponentially with surface pressure in similar ways for all cholesterol fractions. This increase can be explained with a free-area model that relates η_s to the pure DPPC monolayer compressibility and collapse pressure. The elastic modulus, G' , initially decreases with cholesterol fraction, consistent with the decrease in λ expected from the line-active nanodomains, in analogy to 3D emulsions. However, increasing cholesterol further causes a sharp increase in G' between 4 and 5 mol% cholesterol owing to an evolution in the domain morphology, so that the monolayer is elastic rather than viscous over 0.1–10 Hz. Understanding the effects of small mole fractions of cholesterol should help resolve the controversial role cholesterol plays in human lung surfactants and may give clues as to how cholesterol influences raft formation in cell membranes.

surface rheology | isotherms | free-volume model | AFM

Minute fractions of cholesterol lead to dramatic changes in dipalmitoylphosphatidylcholine (DPPC) monolayer morphology (Figs. 1–3) (1, 2) and have equally dramatic effects on monolayer dynamic properties. One weight percent cholesterol reduces the surface viscosity, η_s , of DPPC monolayers by an order of magnitude, and 2 wt% reduces η_s by two orders of magnitude (Figs. 4–6). Atomic force microscopy (AFM) images and micro-rheological data show that the cholesterol is segregated to line-active, locally disordered nanodomains that are dispersed in and separate ordered, primarily DPPC domains. As a result, the monolayer retains many of the features of pure DPPC monolayers including a high collapse pressure, high compressibility, and so on, while having significantly lower surface viscosity. This surface viscosity effect suggests a role for cholesterol in lung surfactant (LS), a lipid–protein monolayer necessary to reduce the surface tension in the lung alveoli during respiration (Fig. S1) (3, 4). At present, even the existence of cholesterol in native LS is questioned, because the lung lavage required to harvest LS inevitably causes blood and cell debris to be coextracted, potentially contaminating LS with cholesterol (5). This lack of consensus over the role of cholesterol is reflected in the composition of replacement lung surfactants for neonatal respiratory distress syndrome (NRDS), which occurs in 20,000–30,000 premature births each year (6). Survanta and Curosurf, two clinically approved animal-extract replacement surfactants for treatment of NRDS, have all cholesterol removed after harvesting. Infasurf, the third clinically approved surfactant, retains 4–5 wt% cholesterol (Table S1) (7, 8). Resolving this controversy is difficult, because there is little information on the effects of small mole fractions of cholesterol on the organization and dynamics of phospholipid monolayers at the

molecular, monolayer, or cell-membrane scale [mitochondrial membranes have ~5 mol% cholesterol and endoplasmic reticulum ~10 mol% (9)]. Cholesterol is also implicated in the formation of stable, 10- to 100-nm “rafts” within the plasma membrane of cells (10, 11), which may serve as platforms for organizing proteins responsible for cell signaling or membrane trafficking. The local viscous, elastic, and line tension properties of the rafts relative to their surrounding membrane likely have important implications for their formation, stability, and function (11).

Materials and Methods

Isotherms. The 1,2-dipalmitoyl-*sn*-glycero-3-phosphocholine (DPPC, R-enantiomer) and dihydrocholesterol (Avanti) with 0.1 wt% Texas Red DHPE [*N*-(Texas Red sulfonyl)-1,2-dihexadecanoyl-*sn*-glycero-3-phosphoethanolamine; Invitrogen] were mixed in the appropriate ratios and diluted to ~0.2 mg/mL in HPLC-grade chloroform (Fischer Scientific) to form a spreading solution. Dihydrocholesterol was used instead of cholesterol to minimize oxidation but has little impact on the nature of the phase behavior (1). The spreading solution was deposited dropwise from a Hamilton syringe onto a custom-built Langmuir trough with two symmetric barriers at 21° C (12). Twenty minutes were allowed for solvent evaporation before film compression. A 15-mm-diameter circular reservoir isolated part of the trough surface to minimize convective drift and help localize the microbuttons (12). A filter paper Wilhelmy plate (Riegler and Kirstein) was used to measure surface pressure.

AFM and Langmuir–Blodgett Deposition. Freshly-cleaved mica substrates (S&J Trading Inc.) connected to a computer-controlled dipping mechanism in a commercial circular NIMA L-B trough (Biolin Scientific, Inc.) were pulled through the monolayer at 5 mm/min at constant surface pressure. Transfer ratios were determined by recording the interfacial area change of the trough during transfer and comparing this to the surface area of the mica substrate. A transfer ratio of 1 means that these areas are equal; only films with transfer ratios of ~1 were examined. The mica substrates were glued to stainless steel discs and affixed to the magnetic holder of an MMAFM-2 AFM

Significance

Replacement lung surfactants have dramatically reduced premature infant mortality owing to respiratory distress syndrome. However, clinical lung surfactant varies widely in composition, and even the existence of cholesterol in native lung surfactants remains controversial. Improving replacement surfactants will require an understanding of each molecular component's role in a film's static and dynamic properties. Here, we show that small cholesterol fractions reduce the viscosity of model lung surfactant interfaces by orders of magnitude while leaving compressibility and collapse unchanged, offering control over surfactant spreadability. Lipid–cholesterol nanodomain complexes are observed, which act as line-active sources of free area to reduce surface viscosity.

Author contributions: K.K., S.Q.C., T.M.S., and J.A.Z. designed research; K.K. performed research; S.Q.C. and J.A.Z. contributed new reagents/analytic tools; K.K., S.Q.C., Z.A.Z., T.M.S., and J.A.Z. analyzed data; and K.K., T.M.S., and J.A.Z. wrote the paper.

The authors declare no conflict of interest.

This article is a PNAS Direct Submission.

¹To whom correspondence should be addressed. E-mail: zasad008@umn.edu.

This article contains supporting information online at www.pnas.org/lookup/suppl/doi:10.1073/pnas.1303304110/-DCSupplemental.

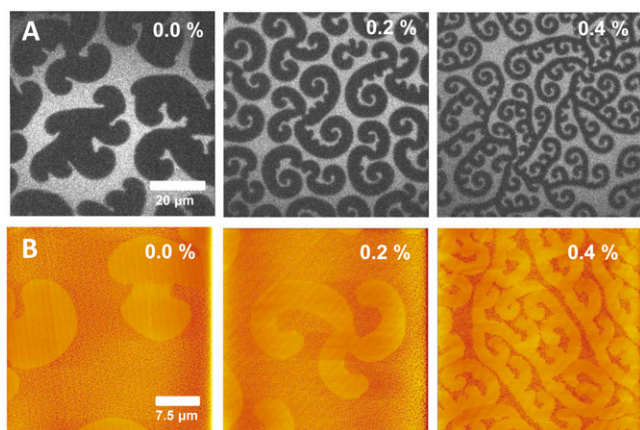


Fig. 1. (A) Epifluorescence images of DPPC monolayers with 0, 0.2, and 0.4 mol% cholesterol at coexistence between the disordered LE (light) and ordered LC (dark) phases. The decreased width and increased length of the LC domain arms is indicative of a decreased line tension between the two phases (1, 2). (B) Corresponding AFM images from monolayers deposited on mica substrates. The LC domains are yellow, corresponding to a nominally greater height, which is due to the greater compliance of the softer LE continuous phase (red-orange). Comparison between *A* and *B* show that the domain shapes are unaltered by the deposition process.

(Digital Instruments) with a cantilever tip (AC160TS; Asylum Research) designed for tapping mode operation.

Interfacial Microrheology. Circular ferromagnetic probes (microbuttons, Fig. 4) of diameter 20 μm , thickness 1 μm , with “button holes” of diameter 3.5 μm were fabricated by photolithography as described elsewhere (13). Briefly, a sacrificial layer (Omnicoat; MicroChem Corp.) was deposited onto a silicon wafer (4 inch; Rockwood) followed by a 1- μm -thick layer of photoresist (SU-8; MicroChem Corp.). The wafer was exposed to UV light through a photomask; the photoresist was developed and washed. A layer of nickel of controlled thickness (either 50 or 150 nm) was deposited via electron-beam evaporation onto one side of the microbutton, followed by a 10-nm layer of gold, and the entire wafer was dipped into a 1.0 mM solution of 1H, 1H, 2H, 2H, perfluorooctanethiol (Sigma) in ethanol to form a hydrophobic self-assembled monolayer on the gold. The microbuttons were released by removing the sacrificial layer with water and cleaned using isopropyl alcohol. The magnetic moments of the microbuttons, $m = (50 \pm 11) \times 10^{-10}$ emu for the 150-nm-thick nickel and $(6.9 \pm 2.3) \times 10^{-10}$ emu (12, 14), were determined by placing the microbuttons on the water/air interface and measuring the rotational response to a known magnetic field.

A uniform magnetic field of magnitude B and orientation θ was generated by the output of two independent pairs of electromagnets controlled by a custom LabVIEW code (12, 14) to exert a controlled torque, L , on a microbutton of moment m and orientation ϕ : $L = mB \sin(\phi - \theta)$. To minimize systematic errors, the direction of the imposed magnetic field was chosen to be perpendicular to the magnetic moment of the microbutton, so that $\theta = (\phi + \pi/2) \pm (\delta\phi - \delta\theta)$ and $L = mB[1 \pm (\delta\phi - \delta\theta)^2]$. To measure the frequency-dependent linear viscoelastic response, a sinusoidal magnetic field was applied to generate a time-varying applied torque, $mBe^{i\omega t}$. The driving torque was kept small enough that the response was linear, with angular displacements limited to a maximum amplitude, $\theta_0 \approx 0.1$ rad. The microbutton orientation $\theta_0(\omega)e^{i(\omega t + \gamma)}$ was determined from bright-field images of the holes in the microbuttons as a function of applied torque, to determine the rotational resistance, $\xi_r^*(\omega) = (mBe^{-i\gamma})/(i\omega\theta_0)$.

From $\xi_r^*(\omega)$, the linear viscoelastic surface moduli, $G_s^*(\omega) = G_s'(\omega) + iG_s''(\omega)$, or equivalently, the complex surface viscosity, $\eta_s^* = G_s^*(\omega)/i\omega$, were obtained from the solution of the hydrodynamic problem of a rotating cylinder within a viscoelastic monolayer atop a viscous subphase (14–17). This calculation assumes the monolayer to behave as a homogeneous, continuum material, whereas the DPPC/cholesterol monolayers exhibit grainy liquid crystalline phases. Nonetheless, the 10- μm probe radius significantly exceeds the characteristic grain sizes (~ 100 nm at 5% to 1 μm at 0.8% cholesterol). Liquid condensed (LC) domains in pure DPPC monolayers have characteristic widths approaching the probe radius yet give results consistent with trends for smaller-grained compositions (Fig. 5). We find similar results when using a

100- μm -diameter probe. Hence, we thus approximate all monolayers as continua.

The resistance ξ_r^* depends on the Boussinesq number Bo , which relates interfacial drag to subphase drag. For purely Newtonian fluids, Bo is given by $Bo = 2\eta_s/\eta a$, wherein a is the microbutton radius, η_s is the surface viscosity, and η is the subphase viscosity, whereas for viscoelastic monolayers $Bo = \frac{2|G_s' + iG_s''|}{\omega\eta} = \frac{2|G_s' + iG_s''|}{\omega\eta}$, in which G_s^* is the subphase modulus, given by $i\omega\eta$ for a Newtonian subphase. For $Bo \ll 1$, the subphase drag dominates, and the rotational resistance is $\xi_r^*(\omega) = (16/3)\eta^*a^3$; when $Bo \gg 1$, $\xi_r^*(\omega) = 4\pi\eta_s^*a^2$ and the drag is dominated by the surface rheology (14). In terms of measured experimental properties, the surface viscosity and elasticity for $Bo \gg 1$ are given by $G_s' = \frac{mB}{4\pi a^2 \theta_0} \cos \gamma$ and $\eta_s = \frac{mB}{4\pi a^2 \omega \theta_0} \sin \gamma$, as $(\eta_s = G_s''/\omega)$.

To ensure that interfacial properties dominated the response, experiments were analyzed only for films with $\xi_r^*(\omega) \gg (16/3)\eta a^3$, for which $Bo \gg 1$ and thus $\xi_r^*(\omega) = 4\pi\eta_s^*a^2$. For aqueous subphases with $\eta \sim 10^{-3}$ N·s/m², the minimum $|G_s' + iG_s''|$ that can be reliably measured with a 10- μm -radius microbutton is of order $G_s' \sim 10^{-8}$ N/m, or $\eta_s^* \sim 10^{-2}$ μN ·s/m at 1 Hz. The maximum measurable surface drag, $|G_s' + iG_s''|$, is limited to ~ 300 μN /m by the maximum torque that can be applied by the electromagnets to microbutton probes with a given magnetic moment. This limits the surface pressure range for cholesterol fractions ≤ 1.6 mol% to about 30 mN/m. Higher mole fractions of cholesterol cause $|G_s' + iG_s''|$ to decrease and allow the surface viscosity and elasticity to be measured up to surface pressures of 50 mN/m or more.

Uncertainties in the measurement of $G_s^*(\omega)$ arise due to statistical variations in the magnetic moment, m , of the microbuttons, the temporal resolution in relating the optical image of the disk to the applied magnetic field, and errors in measuring the phase lag, γ . For primarily viscous films ($G_s'' \gg G_s'$), $\gamma \sim \pi/2$, so that uncertainties in measuring the phase lag cause the relative error in G_s' to be large; for primarily elastic films ($G_s' \gg G_s''$), $\gamma \sim 0$, and the relative error in G_s'' , and hence η_s , is large.

Results and Discussion

DPPC makes up 50–70% of the lipid in lung surfactant (7) and is typical of the zwitterionic phospholipids in cell membranes (11). Fig. 1 shows that as little as 0.2 mol% cholesterol dramatically alters domain shapes in phase-separated monolayers of DPPC (2). Cholesterol decreases the width and increases the length and rotation of the LC domain arms at coexistence, consistent with a decreased line tension, λ , between phases (2). The arm rotation

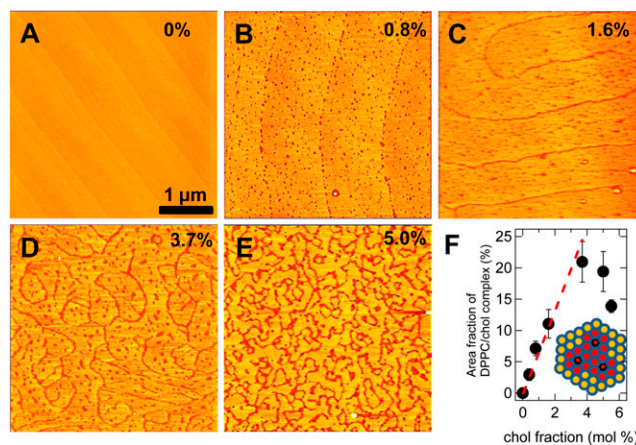


Fig. 2. AFM images of DPPC/cholesterol monolayers transferred to mica substrates at 20 mN/m. (A) Pure DPPC is uniform with minimal height or compliance variations. (B) For 0.8 mol% cholesterol, dispersed 10–100 nm red nanodomains appear, which preferentially locate at the boundaries of the yellow DPPC domains. (C) Increasing cholesterol causes the nanodomains to percolate into lines along the spiral domain boundaries. (D) The 3.7 mol% cholesterol induces linear features that begin to break up the DPPC domains. (E) The 5.0 mol% cholesterol creates a cocontinuous network structure of red and yellow domains. (F) The area fraction of red domains increases linearly with cholesterol fraction up to 3.7 mol%, then saturates. The slope of the line suggests a 6:1 ratio of DPPC to cholesterol in the red domains; a possible packing motif is shown (*Inset*).

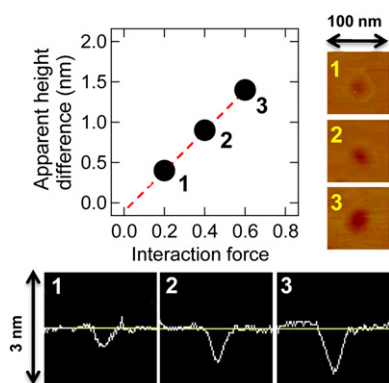


Fig. 3. Contrast in AFM images are convolutions of the variations in sample compliance and sample topography. Varying AFM tip-sample interactions and recording the apparent height variations (line traces at bottom) as a function of the interaction force distinguishes between the two. The apparent height differential between the red nanodomains and background (yellow) matrix decreases with decreasing interaction force (height traces, Lower). Each trace and image corresponds to the forces labeled 1, 2, and 3 on the graph. Extrapolation to zero force suggests that the different domains are similar in thickness and that the image contrast is due to the red nanodomains' being softer and more compliant.

and orientation are a mesoscopic manifestation of the molecular chirality of DPPC (1). AFM images of monolayers transferred to mica (18) (Fig. 1*B*) show that the domain widths decrease from $\sim 5 \mu\text{m}$ for pure DPPC to $\sim 1 \mu\text{m}$ at 0.4 mol% cholesterol.

Monolayers deposited at 20 mN/m (Fig. 2*B–E*), where both DPPC and cholesterol molecules occupy the same molecular area ($\sim 43 \text{ \AA}^2/\text{mol}$, Fig. 5*D*), show 10- to 100-nm-diameter nanodomains that increase in number with increasing cholesterol fraction (red), dispersed within a primarily DPPC matrix (yellow). No such nanodomains are present in the pure DPPC films (Fig. 2*A*). The area fraction of the nanodomains scales linearly with the cholesterol content (Fig. 2*F*) up to 3.7 mol%, giving a cholesterol:DPPC ratio of $1: 5.7 \pm 0.6$, consistent with a stoichiometric ratio of approximately one cholesterol to six DPPC molecules (Fig. 2*F*, *Inset*). The nanodomain area fraction saturates at 3.7 mol% and does not change with further increase in cholesterol fraction.

Nanodomains accumulate along the spiral domain boundaries (Fig. 2*B*) and percolate into linear structures (Fig. 2*C* and *D*) that decorate the boundaries, although the thickness of the linear structures remains similar to the dispersed nanodomain diameter. This preferential location at domain boundaries and the stable, nanometer-scale size of the domains suggest that the cholesterol/DPPC complex is “line-active” (2), while also “soluble” within the LC domains. Further increases in cholesterol lead to increasing area fractions of the nanodomains, which eventually break up the DPPC domains (Fig. 2*E*). By 5 mol%, the nanodomains form a network that breaks up the DPPC domains, decreasing the average DPPC domain size to fractions of a micrometer (Fig. 2*E*).

The contrast in the images in Fig. 2 indicates variations in sample topography and/or local compliance (“softness”). Measuring the apparent height variations in the sample as a function of the tip-sample interaction force (accomplished experimentally by altering the gap between the sample and tip, as discussed in *Supporting Information*) differentiates between variations in topography and compliance (Fig. 3). Fig. 3 shows that the apparent height difference between the red and yellow domains in the monolayer decreases linearly with a decrease in the interaction force, F_{int} . Extrapolation to $F_{int} = 0$ shows that the AFM image contrast is due primarily to the softness of the red nanodomains, rather than to variations in the monolayer thickness. Line traces through the red domains show the triangular shape of the cantilever

tip, suggesting that the apparent width of the red domains is also proportional to F_{int} . As a result, images were taken with minimal tip-sample interaction to estimate the area fraction of the red domains, but this remains a source of error. The greater compliance of the nanodomains is consistent with a more disordered packing, similar to the liquid expanded (LE) phase in Fig. 1, rather than differences in molecular tilt or segregation of the cholesterol or DPPC fractions, because the latter would lead to measurable variations in monolayer height (18).

Interfacial Viscosity and Elasticity. Our highly sensitive micro-rheology technique (12, 14) shows that cholesterol drastically reduces the surface viscosity of DPPC monolayers (Fig. 5). Over the frequency range of 0.1–10 Hz, G'' for DPPC (12) and its mixtures with cholesterol (*Supporting Information*) is linear with frequency, consistent with a constant surface viscosity ($\eta_s = G''/\omega$). However, 1.6 mol% (1 wt%) cholesterol decreases the surface viscosity by an order of magnitude relative to pure DPPC, and 3.7 mol% (2 wt%) decreases the surface viscosity by two orders of magnitude, over the entire range of surface pressure (Fig. 5*A* and *B*).

The surface viscosity depends on both surface pressure, Π , and cholesterol mole percent. At a given surface pressure, the surface viscosity obeys an empirical log-additivity rule that successfully predicts the viscosity of polymer blends (19),

$$\ln \eta_s^0(\phi_r, \Pi) = \phi_r \ln \eta_r^0(\Pi) + \phi_y \ln \eta_y^0(\Pi), \quad [1]$$

as shown in Fig. 5*C*. Here ϕ_r and ϕ_y are the area fractions (analogous to polymer volume fractions in ref. 19) of the red and yellow domains in Fig. 2 and $\eta_r^0(\Pi)$ and $\eta_y^0(\Pi)$ are the surface viscosities of the yellow domains (Fig. 5*A*) and nanodomains. The best fit to Eq. 1 is obtained by setting $\eta_y^0 = \eta_{DPPC}^0$, which shows that the nanodomains are inviscid ($\eta_r^0 \sim 10^{-6} \mu\text{N}\cdot\text{s}/\text{m}$), that is the drag on the nanodomains is dominated by the subphase. Low-viscosity nanodomains suggest a fluid-like, disordered molecular packing as is consistent with AFM images and force spectroscopy (Fig. 3). Effectively, at a given surface pressure, $\ln \eta_s^0 \propto \phi_{DPPC} \ln \eta_{DPPC}^0$.

The relationship between surface viscosity and surface pressure is remarkably insensitive to cholesterol. The surface viscosity for all cholesterol fractions increases exponentially with surface pressure (Fig. 5*A*) or, equivalently, decreasing area/molecule (Fig. 5*B*)—with essentially identical slopes. This exponential increase

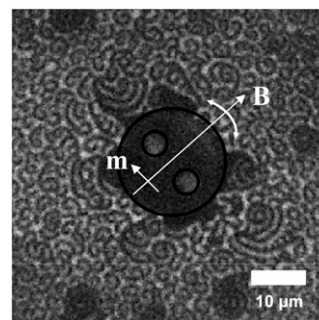


Fig. 4. A circular, ferromagnetic microbutton probe of diameter $20 \mu\text{m}$ and thickness $1 \mu\text{m}$ is pinned by capillary forces within a DPPC/cholesterol monolayer at the air-water interface. Two independent pairs of electro-magnets impose a spatially uniform magnetic field (12, 14) to exert a known torque on the microbutton (*Movie S1*). The magnetic field is imposed nearly perpendicular to the magnetic moment of the microbutton, to minimize the impact of small field misalignment on applied torque. There is no apparent segregation of the phases at the microbutton perimeter; the monolayer is pinned firmly to the microbutton with no slip.

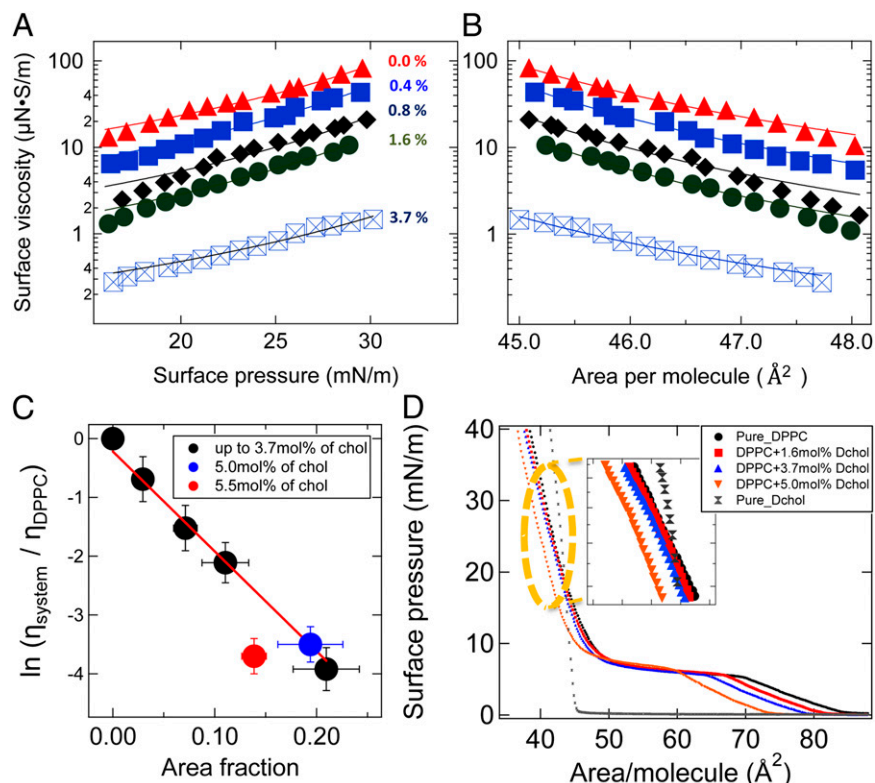


Fig. 5. Surface viscosity vs. surface pressure (A) and surface viscosity vs. area per molecule (B) for mixed DPPC-cholesterol films. The surface viscosity decreases by two orders of magnitude with only 3.7 mol% (2 wt%) cholesterol, but the slope of the curves is unchanged. (C) At any surface pressure, Π , the surface viscosity of the mixed film decreases exponentially with the area fraction of “red” nanodomains in Fig. 2 (Eq. 1). The solid lines in A are fits to Eq. 3, and in B to Eq. 2; both fits work over the entire range of surface pressure (or area per molecule), and the fitting parameters (Table 1) are consistent with the isotherms (D), which show minimal changes up to 3.7 mol% cholesterol. For 5 mol% cholesterol, the film condenses to lower areas per molecule than expected from ideal mixtures, suggesting changes to the molecular packing.

with surface pressure is consistent with a free-area model for the surface viscosity (20–22):

$$\ln \eta_s(\Pi) = \ln \eta_s^0 + \frac{BA_0}{A_f(\Pi)}. \quad [2]$$

The free area, $A_f(\Pi) = A(\Pi) - A_0$, is the difference between the (measured) area $A(\Pi)$ per molecule (Fig. 3D) and the minimum area/molecule, A_0 , for a close-packed phase.

The original, 3D free-volume model assumes condensed phase molecules with van der Waals volume V_0 to move with thermal velocity u , within confining cages of diameter d_0 defined by their nearest neighbors (23). Density fluctuations change cage volumes stochastically, and diffusion occurs when one molecule jumps into the hole left by another molecule, before the original molecule returns to its starting position (23). The probability $P(V_0)$ that the accessible (“free”) volume V_f rearranges to give a void volume V_0 large enough for a molecule to diffuse is given by

$$P(V_0) = \exp[-BV_0/V_f], \quad [3]$$

thus giving a diffusivity

$$D = g \cdot d_0 \cdot u \cdot \exp[-BV_0/V_f] = D_0 \exp[-BV_0/V_f], \quad [4]$$

in which g is a geometric factor (23). The parameter B in Eqs. 3 and 4 accounts for overlaps of free volume and ranges from $1/2 \leq B \leq 1$ (23). We find that the value of B makes little difference in the important fitting parameters of the model (Figs. S2 and S3 and Table S2), so we set $B = 1$.

The free-area model can be adapted for molecules confined to monolayers (or bilayers) of constant mean thickness L (22), via

$$\frac{V_0}{V_f} = \frac{LA_0}{L(A(\Pi) - A_0)} = \frac{A_0}{A_f}. \quad [5]$$

The diffusivity (Eq. 4) can be related to the surface viscosity, η_s , via the Saffmann–Delbrück model (15) for a cylinder diffusing within a viscous monolayer surrounded by a viscous subphase, giving Eq. 2. (details in [Supporting Information](#)).

By expanding $A(\Pi)$ in a Taylor series expansion about the close-packed area $A_0(\Pi_0)$, we can relate the surface viscosity directly to the isotherms:

$$\begin{aligned} A_f &= A(\Pi) - A_0 \approx \left[A_0 + \left(\frac{\partial A}{\partial \Pi} \right) \Big|_{A_0} (\Pi - \Pi_0) \right] - A_0 \\ &= \left(\frac{\partial A}{\partial \Pi} \right) \Big|_{A_0} (\Pi - \Pi_0). \end{aligned} \quad [6]$$

The surface compressional modulus, $K_0 = -A_0 \left(\frac{\partial \Pi}{\partial A} \right)_{T,P} = A_0 \left(\frac{\partial^2 G}{\partial A^2} \right)_{T,P}$, connects the surface viscosity to the shape of the isotherm (Eq. 2):

$$\ln \eta_s = \ln \eta_s^0 + \left(\frac{BK_0}{\Pi_0 - \Pi} \right). \quad [7]$$

Moreover, because K_0 follows directly from the Gibbs free energy G , the dependence of surface viscosity on Π reflects the

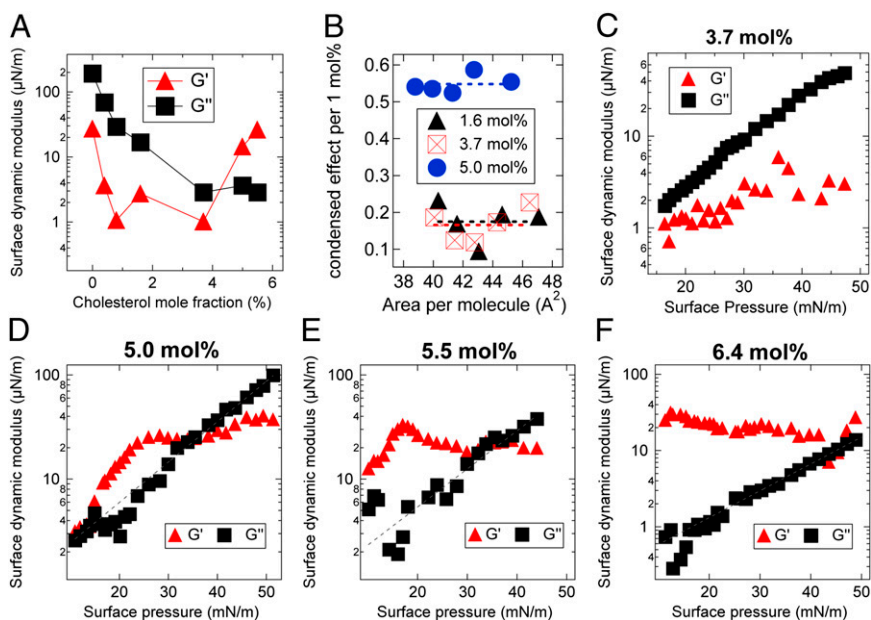


Fig. 6. (A) The elastic modulus, G' , and viscous modulus, G'' , both decrease by orders of magnitude on addition of cholesterol to DPPC monolayers. G'' decreases by two orders of magnitude as cholesterol mole fraction increases from 0 to 3.7 mol%, then plateaus. G' decreases by an order of magnitude at 1 mol% cholesterol, then plateaus, only to increase abruptly between 3.7 and 5.0 mol% cholesterol. (B) The area per molecule of mixed films with 3.7 mol% cholesterol and below is given very nearly by the mole fraction-weighted molecular areas of pure DPPC and cholesterol films. Above 5 mol% cholesterol, however, the average area per molecule of the mixed films is significantly lower than the average of ideally mixed molecules, each adding its pure-component area, suggesting a fundamental change in the molecular organization of the cholesterol–DPPC lattice. (C–F) Surface viscosity increases exponentially with surface pressure for all cholesterol fractions, but with half the slope for ≥ 5 mol% cholesterol. Furthermore, G' becomes much higher for ≥ 5 mol% cholesterol and plateaus at 20 $\mu\text{N}/\text{m}$ (15-fold higher than at 3.7 mol%) above a surface pressure that decreases with mole percent. The cross-over surface pressure (at 1 Hz) from elastic-dominated to viscous-dominated behavior thus increases with cholesterol fraction.

thermodynamic state of the monolayer. For $\Pi \ll \Pi_0$, the free-area model suggests that $\ln \eta_s$ varies linearly with surface pressure,

$$\begin{aligned} \ln \eta_s &= \ln \eta_s^0 + \frac{BK_0}{\Pi_0 \left(1 - \Pi/\Pi_0\right)} \approx \ln \eta_s^0 + \frac{BK_0}{\Pi_0} \left(1 + \Pi/\Pi_0\right) \\ &= \ln \eta_s^* + \frac{BK_0}{\Pi_0^2} \Pi, \end{aligned} \quad [8]$$

as seen in Fig. 5, but $\ln \eta_s$ should diverge as the surface pressure approaches Π_0 .

The solid lines through the data in Fig. 5A and B show that the free-area model (Eqs. 7 and 2, respectively) captures all cholesterol fractions and surface pressures. Best-fit values of A_0 , K_0 , and π_0 are identical for all cholesterol fractions up to 3.7 mol%, within the error of the measurement (Table 1). Moreover, all best-fit values are physically reasonable. The mean value of Π_0 , 64 ± 2 mN/m, is roughly equal to the collapse pressure of DPPC/cholesterol monolayers (24). The best-fit value of the close-packed molecular area, $A_0 = 38.7 \pm 0.4 \text{ \AA}^2$, corresponds to the interfacial area occupied by two close-packed, all-*trans* alkane chains in fatty acid monolayers (18, 25), which is approximately the area per molecule at monolayer collapse (4). The best-fit compressibility K_0 , 206 ± 4 mN/m, agrees with our measured isotherms (Fig. 3D) and literature values for DPPC monolayers (24).

Increasing surface pressure adds to $\ln \eta_s$ with a slope identical to pure-phase DPPC viscosities, irrespective of cholesterol mole percent; that is, $\ln \eta_s(\Pi) \propto \phi_{\text{DPPC}} \ln \eta_{\text{DPPC}}(\Pi)$ over the entire range of surface pressure. These observations are consistent with the hypothesis that the yellow regions in Figs. 1 and 2 correspond to pure DPPC, with the softer, less-ordered nanodomains acting as constant sources of “free area,” independent of the surface

pressure. The similarity of the isotherms, and the values of A_0 , K_0 , and π_0 are consistent with a relatively unchanged molecular organization of the DPPC domains (yellow) up to 3.7 mol% cholesterol. Because $K_0 = A_0(\partial^2 G/\partial A^2)_{T,P}$ is constant over the range of cholesterol concentrations up to 3.7 mol%, the thermodynamic state of the monolayer should be constant as well. The free-area model also suggests that the surface viscosity should diverge as $A(\Pi)$ approaches A_0 (or as Π approaches Π_0); however, we cannot investigate this region because our current instrument is limited to surface viscosity $\leq 100 \mu\text{N}\cdot\text{s}/\text{m}$. Previous investigations of lipid mixtures with larger-scale needle viscometers have shown rapid increases in surface viscosity at higher surface pressures consistent with Eqs. 2 and 7 (26, 27).

Finally, we note that we have used free-area models to treat viscoelastic and semicrystalline monolayers, whereas the original free-volume models were developed for small-molecule liquids. Our standing hypothesis (14) is that LC–DPPC is purely viscous

Table 1. Fitting parameters for Eqs. 2 and 7 for surface viscosity data in Figs. 5 and 6

Cholesterol, mol%	η_s^0 , $\mu\text{N}\cdot\text{s}/\text{m}$	A_0 , \AA^2	π_0 , mN/m	K_0 , mN/m
0.0	0.257	38.4	64	198
0.4	0.093	38.9	63	208
0.8	0.042	38.9	63	209
1.6	0.021	39.0	62	206
3.7	0.006	38.1	67	207
5.0	0.075	34.3	74	148
5.5	0.012	33.9	78	158
6.4	0.018	33.8	79	158

The gray background highlights the differences in fitting parameters for cholesterol fractions ≥ 5.0 mol%.

over the range of respiration frequencies, and that the measured surface viscosity of the mixed DPPC/cholesterol film is dominated by the response of the DPPC domains (Fig. S4). It is the finite line tension between discrete DPPC LC domains that gives rise to a mesoscopic elastic response. Under this assumption, we would expect the free-area model to hold for the internal phase, and indeed find consistent results here.

Crossovers Between Viscous-Dominated and Elastic-Dominated Behavior. Pure DPPC monolayers are only weakly viscoelastic; the elastic modulus, G' , is an order of magnitude lower than the loss modulus, $G'' = \omega\eta_s$, at 1 Hz (Fig. 6A). As with η_s , G' decreases by an order of magnitude as cholesterol fraction increases up to ~ 1 mol% cholesterol, so that the monolayer remains primarily viscous at 1 Hz. Between 1 and 3.7 mol% cholesterol, however, G' plateaus, then increases sharply between 3.7 and 5 mol% cholesterol, whereupon the films are predominantly elastic ($G' \gg G''$) at 1 Hz and $\Pi = 20$ mN/m (at sufficiently high frequencies, G'' will likely be greater than G').

We previously hypothesized that LC-DPPC responds like a concentrated, 2D emulsion (14) whose viscosity is dominated by the internal (LC-DPPC) phase, and whose elasticity arises due to the line tension of the nanodomain phase at the LC grain boundaries. In 3D emulsions, when the interior phase droplets stabilized by surfactant layers are deformed by shear, an opposing capillary pressure and recoverable strain is generated, leading to an effective elastic modulus, $G' \sim \gamma/R$, in which γ is the surface tension and R the radius of the emulsion droplets (14). The monolayer analog is $G' \sim \lambda/R$, where R is the characteristic domain size and λ is the line tension (14), which gave reasonable values for λ in pure LC-DPPC monolayers, despite the difficulty of performing truly quantitative analysis due to the nontrivial domain shapes and anisotropic line tension.

Adding cholesterol decreases domain widths (Fig. 1) and introduces nanodomains along domain boundaries (Fig. 2), which would be consistent with decreasing λ (2). We hypothesize that the initial decrease in G' with cholesterol is likely due to this decrease in λ because the domain sizes (AFM images in Fig. 2) do not change significantly from 0.8 to 1.6 mol%. However, λ likely saturates once nanodomains form continuous lines along the grain boundaries (≥ 1.6 mol% cholesterol, Fig. 2C), at which point G' plateaus at 2–3 $\mu\text{N}/\text{m}$ (Fig. 6A and C). Further increases in cholesterol lead to a cocontinuous morphology at 5 mol%, wherein the effective domain radius decreases 10-fold from its value at 1.6 mol%. The 10-fold increase in G' , to a value ~ 20 $\mu\text{N}/\text{m}$ (independent of cholesterol fraction or Π), is consistent with this decreased domain size R at constant λ (Fig. 6D–F) and constant (or decreasing) nanodomain area fraction (Fig. 5C).

For 5.0 mol% cholesterol and greater, over the same range of surface pressure, $G' \gg G''$, and the scatter in G'' is large (Fig. 6D–F). G'' saturates, along with the fraction of red nanodomains in the AFM images (Fig. 2F), for 5.0 mol% and greater. The elasticity saturates for higher cholesterol content; at higher surface pressures, the elasticity plateaus at 10–20 $\mu\text{N}/\text{m}$ for all cholesterol fractions over 3.7 mol%. The saturation value of G' is similar to what we measured for G' of pure DPPC at 20 mN/m surface pressure, although G'' is two orders of magnitude smaller. Whereas $G' \gg G''$ at low surface pressures, this changes with increasing surface pressure; $\ln(G'')$ increases linearly with surface pressure whereas $\ln(G')$ saturates, leading to a crossover at higher surface pressures. Even though the surface viscosity increases exponentially with surface pressure, for 6.4 mol% cholesterol, the surface viscosity at 55 mN/m is ~ 2 $\mu\text{N}\cdot\text{s}/\text{m}$, compared with ~ 30 $\mu\text{N}\cdot\text{s}/\text{m}$ at 20 mN/m surface pressure for pure DPPC.

In addition, distinct, qualitative changes in both the rheology and the isotherms suggest that fundamental changes in the monolayer organization occur between 3.7 and 5.0 mol%. Surface viscosity increases exponentially with Π , as expected, but with half

the slope measured for 3.7 mol% and below. Furthermore, free-area model-fitting parameters are consistent among films with ≥ 5.0 mol% cholesterol fraction yet differ from the self-consistent parameters obtained for films below 5.0 mol% (Table 1). In particular, fits to the free-area model for the high-cholesterol films show smaller close-packed molecular area A_0 , a higher surface pressure Π_0 to achieve close-packing, and greater compressibility.

These rheological changes arise just as molecular condensation becomes evident in the isotherms (Fig. 5D): For ≤ 3.7 mol%, both cholesterol and DPPC add an essentially ideal (pure component) area per molecule to the monolayer, whereas a dramatic reduction in area per molecule is evident at 5 mol% and higher. DPPC has a large polar headgroup and relatively small, ordered, alkane tailgroups, causing DPPC molecules to tilt to accommodate the frustration between disparate areas per headgroup vs. tailgroups (28–30). Cholesterol, on the other hand, has a relatively small –OH headgroup relative to the bulky sterol ring tailgroup, giving it an inverted cone shape at the air–water interface. The complementary shapes of cholesterol and DPPC may allow cholesterol to intercalate between the tilted chains of DPPC in the nanodomain phase, decreasing the DPPC tilt, as is the case for palmitic acid (28, 29) and hexadecanol (29, 30). Decreasing the tilt leads to a decrease in the molecular area of the mixed film relative to the individual films (Fig. 6B). The similar saturated alkyl chains of both PA and hexadecanol drive cocrystallization with DPPC, and therefore greater surface viscosities (27, 30, 31). By contrast, the sterol ring of cholesterol cannot pack into the alkane lattice of DPPC and thus degrades the DPPC crystal, leading to disordered, low-viscosity nanodomains, which lowers the surface viscosity of the mixed films as $\ln \eta_s \propto \phi_{\text{DPPC}} \ln \eta_{\text{DPPC}}$.

Conclusions

Small mole fractions of cholesterol profoundly alter the morphology and dynamics of phospholipid monolayers. Cholesterol segregates into line-active nanodomains of a 6:1 DPPC:cholesterol complex that lowers surface viscosity by orders of magnitude, by introducing sources of free area for the film. Rheology and isotherm measurements for films with ≥ 5 mol% cholesterol suggest fundamentally different molecular organization; the nanodomains percolate into linear structures that form a bicontinuous network with the DPPC domains.

Similar small fractions of cholesterol also induce the same order of magnitude changes in the surface viscosity of replacement lung surfactants (Fig. S1), which suggests a possible physiological role for cholesterol. Upon exhalation, that is, at small alveolar area and high surface pressure, the exponential increases in surface viscosity should minimize the Marangoni flow that would otherwise occur due to surface tension gradients between the alveoli and the bronchi. At the ~ 1 -s time scales common for respiration, the elastic resistance to flow that occurs with increasing cholesterol should also oppose any Marangoni flow. Upon inhalation, and large alveolar area, lower surface pressures are associated with exponentially lowered viscosity, as would be needed to quickly cover an expanding alveolar interface. Because cholesterol at these small mole fractions does not change the monolayer collapse pressure or isotherms, but provides two orders of magnitude less resistance to spreading, we suggest that an optimized surfactant should contain cholesterol.

In addition, DPPC films with > 5 mol% cholesterol have a significant elastic component over the ~ 1 -s time scales common to respiration. If a film is primarily viscous over this time scale, microstructural elements in the film have time to relax and rearrange. Films that are primarily elastic over this time scale, however, store deformational energy and work to “undo” the deformations imposed previously. On exhalation, the surfactant films may store deformation energy elastically, making it easier for the alveoli to reexpand on inhalation. In this picture, low surface viscosities would provide a minimal drag on this reexpansion.

At high surface pressures, a high surface viscosity coupled with an elastic response may slow the kinetics of 3D buckling that occurs on monolayer collapse, wherein jerking motions may reflect overcoming the elastic response (32–34). Understanding the effects of cholesterol will enable these ideas to be tested by providing a simple way to alter monolayer mechanical properties by orders of magnitude with only subtle changes in lung surfactant composition and pressure-area iso-

therms. More broadly, understanding how lipid/cholesterol complexes promote low-line tensions that stabilize dispersed nanodomains may give clues to the mechanisms that stabilize similarly sized “rafts” in more complex lipid–cholesterol mixtures in cell membranes (11).

ACKNOWLEDGMENTS. The authors thank Coralie Alonso and Siegfried Steltenkamp, who helped initiate this project. This work was supported by National Institutes of Health Grant HL-51177.

- McConnell HM (1991) Structures and transitions in lipid monolayers at the air-water interface. *Annu Rev Phys Chem* 42:171–195.
- Weis RM, McConnell HM (1985) Cholesterol stabilizes the crystal-liquid interface in phospholipid monolayers. *J Phys Chem* 89(21):4453–4459.
- Bernardino de la Serna J, Perez-Gil J, Simonsen AC, Bagatolli LA (2004) Cholesterol rules: Direct observation of the coexistence of two fluid phases in native pulmonary surfactant membranes at physiological temperatures. *J Biol Chem* 279(39):40715–40722.
- Zasadzinski JA, Stenger PC, Shieh I, Dhar P (2010) Overcoming rapid inactivation of lung surfactant: analogies between competitive adsorption and colloid stability. *Biochim Biophys Acta* 1798(4):801–828.
- Vockeroth D, et al. (2010) Role of cholesterol in the biophysical dysfunction of surfactant in ventilator-induced lung injury. *Am J Physiol Lung Cell Mol Physiol* 298(1):L117–L125.
- Pérez-Gil J (2008) Structure of pulmonary surfactant membranes and films: The role of proteins and lipid-protein interactions. *Biochim Biophys Acta* 1778(7–8):1676–1695.
- Bernhard W, et al. (2000) Commercial versus native surfactants. Surface activity, molecular components, and the effect of calcium. *Am J Respir Crit Care Med* 162(4 Pt 1):1524–1533.
- Braun A, et al. (2007) A freeze-fracture transmission electron microscopy and small angle x-ray diffraction study of the effects of albumin, serum, and polymers on clinical lung surfactant microstructure. *Biophys J* 93(1):123–139.
- Jamieson GA, Robinson DM (1977) *Mammalian Cell Membranes* Butterworth, London.
- Veatch SL (2007) From small fluctuations to large-scale phase separation: lateral organization in model membranes containing cholesterol. *Semin Cell Dev Biol* 18(5):573–582.
- Lingwood D, Simons K (2010) Lipid rafts as a membrane-organizing principle. *Science* 327(5961):46–50.
- Kim K, Choi SQ, Zasadzinski JA, Squires TM (2011) Interfacial microrheology of DPPC monolayers at the air-water interface. *Soft Matter* 7(17):7782–7789.
- Choi SQ, et al. (2011) Synthesis of multifunctional micrometer-sized particles with magnetic, amphiphilic, and anisotropic properties. *Adv Mater* 23(20):2348–2352.
- Choi SY, Steltenkamp S, Pascall AJ, Zasadzinski JA, Squires TM (2011) Active microrheology of phospholipid monolayers: Seeing stretching, flowing, yielding and healing. *Nat. Comm.* 2:312.
- Saffman PG, Delbrück M (1975) Brownian motion in biological membranes. *Proc Natl Acad Sci USA* 72(8):3111–3113.
- Wurlitzer S, Schmiedel H, Fischer TM (2002) Electrophoretic relaxation dynamics of domains in Langmuir monolayers. *Langmuir* 18(11):4393–4400.
- Hughes BD, Pailthorpe BA, White LR (1981) The translational and rotational drag on a cylinder moving in a membrane. *J Fluid Mech* 110:349–372.
- Viswanathan R, Madsen LL, Zasadzinski JA, Schwartz DK (1995) Liquid to hexatic to crystalline order in Langmuir-Blodgett films. *Science* 269(5220):51–54.
- Utracki LA (1991) On the viscosity-concentration dependence of immiscible polymer blends. *J Rheology* 35(8):1615–1637.
- Sacchetti M, Yu H, Zografis G (1993) Inplane steady shear viscosity of monolayers at the air-water interface and its dependence on free area. *Langmuir* 9(8):2168–2171.
- Alonso C, Zasadzinski JA (2004) Linear dependence of surface drag on surface viscosity. *Phys Rev E Stat Nonlin Soft Matter Phys* 69(2 Pt 1):021602.
- Galla HJ, Hartmann W, Theilen U, Sackmann E (1979) On two-dimensional passive random walk in lipid bilayers and fluid pathways in biomembranes. *J Membr Biol* 48(3):215–236.
- Cohen MH, Turnbull D (1959) Molecular transport in liquids and glasses. *J Chem Phys* 31:1164–1169.
- Albrecht O, Gruler H, Sackmann E (1981) Pressure-composition phase diagrams of cholesterol/lecithin, cholesterol/phosphatidic acid, and lecithin/phosphatidic acid mixed monolayers: A Langmuir film balance study. *J. Coll. Int. Sci.* 79(2):319–338.
- Kaganer VM, Mohwald H, Dutta P (1999) Structure and phase transitions in Langmuir monolayers. *Rev Mod Phys* 71(3):779–819.
- Alonso C, Waring A, Zasadzinski JA (2005) Keeping lung surfactant where it belongs: Protein regulation of two-dimensional viscosity. *Biophys J* 89(1):266–273.
- Ding JQ, Warriner HE, Zasadzinski JA (2002) Viscosity of two-dimensional suspensions. *Phys Rev Lett* 88(16):168102.
- Bringezu F, Ding JQ, Brezesinski G, Zasadzinski JA (2001) Changes in model lung surfactant monolayers induced by palmitic acid. *Langmuir* 17(15):4641–4648.
- Lee KYC, et al. (2002) Influence of palmitic acid and hexadecanol on the phase transition temperature and molecular packing of dipalmitoylphosphatidyl-choline monolayers at the air-water interface. *J Chem Phys* 116(2):774–783.
- Alonso C, Bringezu F, Brezesinski G, Waring AJ, Zasadzinski JA (2005) Modifying calf lung surfactant by hexadecanol. *Langmuir* 21(3):1028–1035.
- Alonso C, et al. (2004) More than a monolayer: relating lung surfactant structure and mechanics to composition. *Biophys J* 87(6):4188–4202.
- Lipp MM, Lee KYC, Takamoto DY, Zasadzinski JA, Waring AJ (1998) Coexistence of buckled and flat monolayers. *Phys Rev Lett* 81(8):1650–1653.
- Pocivavsek L, et al. (2008) Stress and fold localization in thin elastic membranes. *Science* 320(5878):912–916.
- Pocivavsek L, et al. (2008) Lateral stress relaxation and collapse in lipid monolayers. *Soft Matter* 4(10):2019–2029.